Measurement Science and Technology

Characterization of microstructures of specialty optical fibers for electric field sensing by propagation-based X-ray phase-contract tomography

To cite this article before publication: Marcos V. Colaço *et al* 2020 *Meas. Sci. Technol.* in press https://doi.org/10.1088/1361-6501/abd365

CHARACTERIZATION OF MICROSTRUCTURES OF SPECIALTY OPTICAL FIBERS FOR ELECTRIC FIELD SENSING BY PROPAGATION-BASED X-RAY PHASE-CONTRAST MICROTOMOGRAPHY

M. V. Colaço[a], A. R. Camara[b,c] L. P. Nogueira[d], I. C. S. Carvalho[e], W. Margulis[f,g], R. C. Barroso[a]

[a] *Laboratory of Applied Physics to Biomedical and Enviromental Science / Rio de Janeiro State University, Rio de Janeiro, Brazil*
[b] *Laboratory of Research in Fiber Optics, Physics Institute, Quantum Electronics Department, Rio de Janeiro State University, Rio de Janeiro, Brazil*
[c] *Electronic Engeneering Graduation Program (PEL), - Rio de Janeiro State University, Rio de Janeiro, Brazil*
[d] *Oral Research Laboratory, Institute of Clinical Dentistry, University of Oslo, Oslo, Norway*
[e] *Department of Physics, Pontifícia Universidade Católica do Rio de Janeiro (PUC-Rio), Rio de Janeiro, Brazil*
[f] *Department of Fiber Optics, Acreo Swedish ICT AB, Electrum 236, Stockholm, Sweden*
[g] *Department of Applied Physics, KTH, 10691 Stockholm, Sweden*

E-mail: mvcolaco@uerj.br
mvcolaco@gmail.com

ABSTRACT: In this work, we present a quantitative (statistical) 3D morphological characterization of optical fibers used in electric field sensing. The characterization technique employs propagation-based X-ray phase-contrast microcomputed tomography (micro-CT). Particularly, we investigate specialty optical fibers that contain microstructured holes that are electrooptically modified by thermal poling to induce second-order nonlinear effects (SONE). The efficiency of SONE is reflected in the characterization parameter V_π, which is highly dependent on the dimensions of the fiber. The fiber microstructures must be uniform to allow the fabrication of reproducible devices. The results obtained using the micro-CT technique showed that an uncertainty of ±1.7% arises in the determination of the expected value of the voltage that causes a change in the phase of the electromagnetic wave equal to π rad (V_π), showing a great advantage when it is compared with other techniques e.g. SEM, which would need at least 1000 images of the cross-section of the optical fiber taken in different points making the process more expensive and time consuming.

KEYWORDS: Optical fiber, Poling, Phase contrast micro-CT, Synchrotron radiation.

Contents

1. Introduction

Microstructured fused silica optical fibers can be used in pulse selection systems, electric field sensors, and phase-modulators, through the creation of an effective second-order nonlinearity by thermal poling. In this electrooptical modification of optical fibers process, the features of the microstructures of the fibers play an important role in the final value of the second-order susceptibility and, consequently, in the final value of $V\pi$, that is the voltage that shall be applied to the fiber to achieve the optical commutation. Thus, the geometrical parameters of the optical fiber, e.g., size, shape, and distances among the microstructures must not have large fluctuation [1-8].

There are some very well-known techniques as AFM (Atomic Force Microscope) and SEM (Scanning Electron Microscopy) that can be used to measure these microstructures with good accuracy but only for the cross-section of the fiber. In these cases, to analyze a longer piece of fiber one needs to repeat several times all imaging processes as well as the preparation of the fiber in the attempt to estimate the fluctuation

in the geometrical parameters of the fiber. It makes the process very expensive and time-consuming [9, 10].

Among the techniques that can be applied in microstructured optical fiber characterization using 3D analysis, the most promising one is the microcomputed tomography (micro-CT), since it is non-destructive, easy to prepare for scanning and can provide for sub-micrometric pixel size. In the last years, micro-CT has been used as the main technique to 3D analysis applied in different research areas, including as a metrology tool. The main use of this technique as a qualitative tool is for visualization of internal structures of the sample and its changes, in any direction, either in their natural state or previously treated. As quantitative tool the micro-CT provides dimensional measurements of radius, distances and shapes, for example [11-16].

X-ray micro-CT with submicrometric pixel size has already been applied to characterize a hollow-core photonic bandgap fiber and preforms, as well as the bond quality at the joint between two fusion-spliced hollow-core fibers [17]. Another recent work has used micro-CT to investigate the feasibility of using embedded optical fibers in polymer matrix composite laminates, to characterize delamination caused by low-velocity impact [18].

Synchrotron radiation micro-CT (SR micro-CT) technique offers significant advantages, such as a wide energy range, high flux, small source size and beam divergence and it provides short acquisition times with high signal-to-noise ratios at high spatial resolution. Moreover, the high degree of spatial coherence allows one to carry out a scan increasing the phase-contrast effect [19-22].

The aim of this work is, through the SR micro-CT technique, to study the uniformity of a microstructured optical fiber used for poling and to simulate possible abnormalities of geometrical parameters (size, shape, and distances among the microstructures) along the fiber. Moreover, the fluctuation of the electrical potential recorded on the fiber after poling was estimated.

2. Materials and Methods

2.1 Thermal poling process in the optical fiber and COMSOL simulation

In general, glasses are centrosymmetric. Because of this symmetry of inversion, second-order nonlinear effects are forbidden, since the second-order susceptibility $\chi^{(2)}$ is identically zero. In order to create an effective second-order nonlinear coefficient ($\chi^{(2)}_{eff}$) thermal poling can be used, a technique which consists of creating a permanent strong electric field (~GV/m) in the glass by the application of high voltage (~kV) at high temperature [23].

The optical fiber used in this work (model F051007-1C, single mode at 1.55 μm, produced by RISE Acreo, Sweden) is made with fused silica glass, which contains Na^+ and Li^+ ions that are uniformly distributed in its matrix. Furthermore, the fiber has two holes, located close to the fiber core, that will be filled, after the characterization processes, with BiSn (52%, 48% respectively) to be used as electrodes to apply a high voltage (~5kV) in the presence of high temperature in the thermal poling process.

A description of thermal poling of fibers is found in [23-27]. The voltage necessary for switching the poled fiber in an interferometric system is given by $V_\pi = d \cdot \lambda \cdot n_0 / \chi^{(2)}_{eff} \cdot L$, where d is the distance between the holes, λ is the wavelength of the light

source, n_0 is the refractive index of the core of the fiber and L is the length of the fiber. In order to analyze the role of the distance between the holes of the fiber in the final value of $\chi^{(2)}_{eff}$, and, consequently the value of V_π, simulations of thermal poling process [23] were performed in two different situations: i) changing the radius of the holes with a fixed center-to-center distance (holes to core of the fiber) and ii) varying the distance between the center of the holes. In both situations, the variation was ± 2.5 μm in steps of 0.5 μm, starting from the original values of F051007-1C fiber. The geometrical parameters used to perform the simulations of $\chi^{(2)}_{eff}$ are shown in table 1.

Table 1: Geometrical parameters used in the simulations measured using an optical microscope image of the cross-section of the optical fiber.

Parameter	Input data
Fiber diameter	125 μm
Core diameter	5 μm
Holes diameters	27 μm
Distance between core and hole 1 centers	24.2 μm
Distance between core and hole 2 centers	29.2 μm
Separation between holes (edge-to-edge), d	28.4 μm

The solutions given by this model are based on the COMSOL Multiphysics solution of the transport of diluted species problem (TDSP) when it is influenced by the application of an external DC electric field for the i-th ion, given by equation 1.

$$\frac{\partial c_i}{\partial t} + \nabla \cdot \left(- D_i \nabla c_i - z_i \mu F c_i \nabla V \right) = R_i \quad (1)$$

where c is the concentration of the diluted species, D is the diffusivity, z is the charge, μ is the ionic mobility, F is Faradays constant, V the electric potential and R the consumption or production rate. The electric potential distribution and electric field were obtained from Maxwell's equations in the electrostatics regime.

2.2 Scanning Electron Microscopy (SEM)

An emission scanning electron microscopy (SEM) was used for the morphological characterization of the cross-section of F051007-1C fiber. As it gives high-resolution 2D images, a 3 cm section of fiber was cut in eight pieces to determine the average diameters of the fiber and the holes for each piece with a 600x magnification in order to estimate the homogeneity of the size and shape of the microstructure for a whole section. The results were used as a reference to compare them with the micro-CT images since on the one hand, SEM achieves higher magnification while on the other hand micro-CT gives 3D images of a whole section of the optical fiber.

The microscope used in this work was a JEOL model JSM-6510LV. The equipment is located in the Laboratory of Scanning Electron Microscopy at the Institute of Chemistry of the Rio de Janeiro State University.

2.3 Synchrotron micro-CT image at IMX Beamline

The sample was imaged at the IMX beamline, at LNLS (National Synchrotron Light Source), Campinas, Brazil. This beamline has an electron source size of 391 μm x 97 μm and beam divergence of 808 μrad x 26 μrad. Synchrotron radiation is extracted

from bending magnet D6, which has a magnetic field of 1.67 T and a bending radius of 2.736 m. This beamline can operate in either a white beam or a monochromatic beam. The sample is mounted on a high precision stage with 6 degrees of freedom including two linear stages with less than 1 μm resolution for positioning the sample in the detector field of view. Undesirable low energy X-rays can be blocked by applying a combination of silicon filters available. The process of sample alignment is done semi-automatically by an automated script that precisely aligns (within one pixel of precision) the sample onto the rotation axis provided that the sample's region of interest is inside the field-of-view under 180 degrees of rotation. [28].

The scan was carried out in white beam mode with an energy spectrum ranging from 5 keV to 20 keV with a photon flux at the sample position of approximately 10^{15} photons/s. The sample was imaged by the acquisition of 1000 equally spaced projections over 180 degrees rotation of the sample with an exposure time of 0.650 s per projection. For this measurement, a delay time was added between the end of each rotation step and the opening of the shutter to avoid sample movement effects. The total scan duration was approximately 15 minutes.

Propagation-based X-ray phase-contrast computed tomography was implemented using a 10 cm sample-detector distance to increase the phase-contrast effect, making possible the use of a phase retrieval algorithm [29]. The beamline setup (Figure 1) is composed of a 14-bit cooled high-resolution CCD camera attached to a microscope. This camera has a sensor size of 2048 x 2048 pixels, with an isotropic pixel size of 7.4 μm. A 10x objective lens was used, yielding a field of view of 1.7 mm x 1.7 mm, with a final pixel size of 0.82 μm. Precision motors allow for a precise positioning of the sample in

the beam, as well as for the alignment of the sample and the rotation for the projection acquisitions. The setup is also composed of an automatic sample exchanger, allowing for exchanging up to 20 samples without the need for manual handling of the samples.

All projection images were stacked into a single HDF5 format. A conventional filtered back-projection reconstruction algorithm was used with PYRAFT software developed by the LNLS team [30,31].

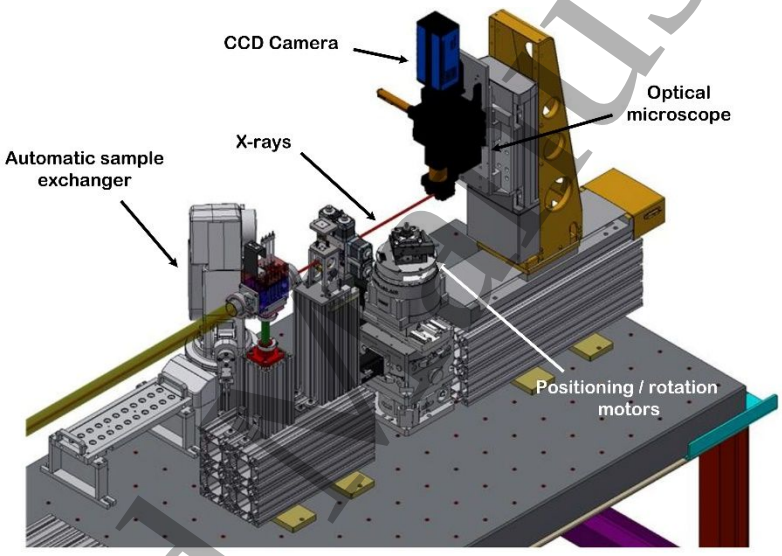

Figure 1: Setup of the experimental hutch at IMX beamline.

2.4 Rendering process and virtual measurements

Avizo 9.4 software (https://www.fei.com/sofware/avizo-for-materials-science/) was used for 3D rendering and analysis. An important step before structure segmentation is the reduction of noise in the reconstructed images. Different filters were tested to obtain better images and preserve borders between holes and the fiber matrix. For this purpose, a non-local means filter was applied to all the data sets.

Afterwards, the 3D volume was segmented by applying a watershed segmentation tool, where gradient images were created to delimitate borders between the exterior and the interior of the fiber and also between the hollow structures (hole 1 and hole 2) and the fiber matrix to separate them as different objects [32].

After checking the results of the generated objects, each one was analyzed. The extracted information for each slice was: the equivalent diameter, the eccentricity, the Feret diameter, and the barycenter coordinates; the later one was used to obtain the values for the distance between the borders of the holes to the center of the fiber.

3. Results

3.1 Optical fiber structure analysis

The fiber and the holes diameters were measured in two directions in a set of pieces of F051007-1C using a SEM. An example of these measurements is shown by the yellow lines in figure 2. The statistical analysis of the SEM measurements in the fiber results is a mean diameter of 125.1 μm and a standard deviation (SD) of 1.4 μm (n = 16). For the diameter of hole 1, the mean value is 24.6 μm with SD of 0.5 μm and for hole 2, the mean value is 24.4 μm with SD of 0.7 μm (n = 32). The resolution of the SEM is about 10 nm and the statistical error about 1 μm for the fiber and 0.5 μm for the holes. The coefficient of variation (CV) for each measurement (the ratio of the standard deviation to the mean value) allows quantifying and comparing the data dispersion in relation to the mean value. The CV's are 1.2%, 2.3% and 3.0% for the fiber diameter, hole 1 and hole 2, respectively.

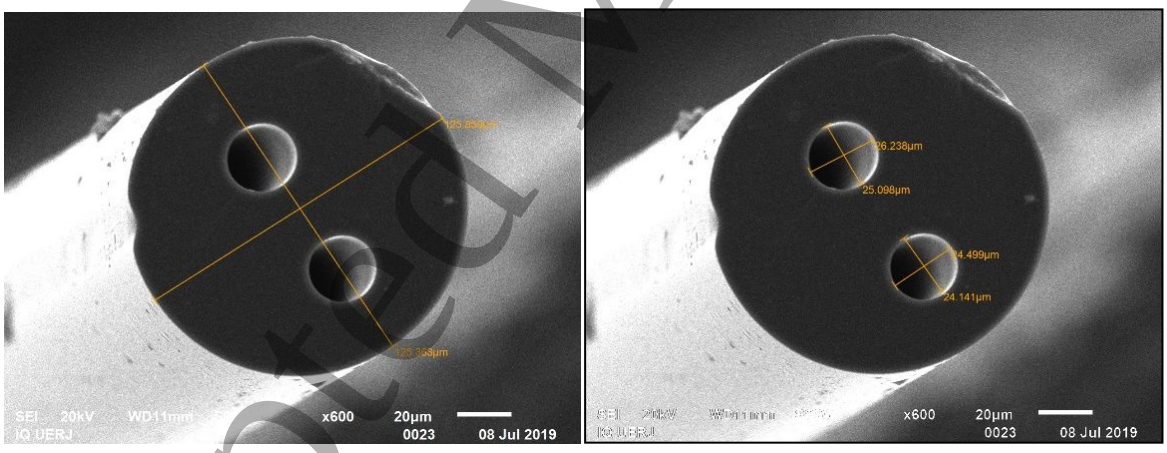

Figure 2: Example of micrographs with measurements of the diameter of the fiber (left) and the holes (right) made in the vertical and horizontal axes (yellow lines). For this piece of fiber, the obtained values for the fiber diameter were 125.86 μm in the horizontal axis and 125.36 μm in the vertical axis. The diameters of the upper hole were 26.24 μm and 25.10 μm and in the lower hole were 24.50 μm and 24.14 μm in horizontal and vertical axes respectively.

For SR micro-CT experiment, a piece of optical fiber was scanned, and the length of 0.820 mm was used to perform the analyses (1000 slices). With sample-to-detector distance fixed at 10 cm, the filtered back-projection (FBP) reconstruction of the datasets showed apparent high magnitudes of the phase effect (figure 3a) and allowed good phase retrieval results (figure 3b). The core of the fiber is not easy to identify since it has a similar density, absorption and refractive index compared to the fiber matrix. Without phase retrieval, the core was not clearly revealed even by adjusting the threshold of the image. However, after the phase retrieval processing and using a colormap, it was possible to visualize the core, indicated in the figure 3b by the yellow arrow and in the figure 3c by the black arrow. Due to the small size of the core compared to pixel size it was not possible apply segmentation process to accurately define its shape.

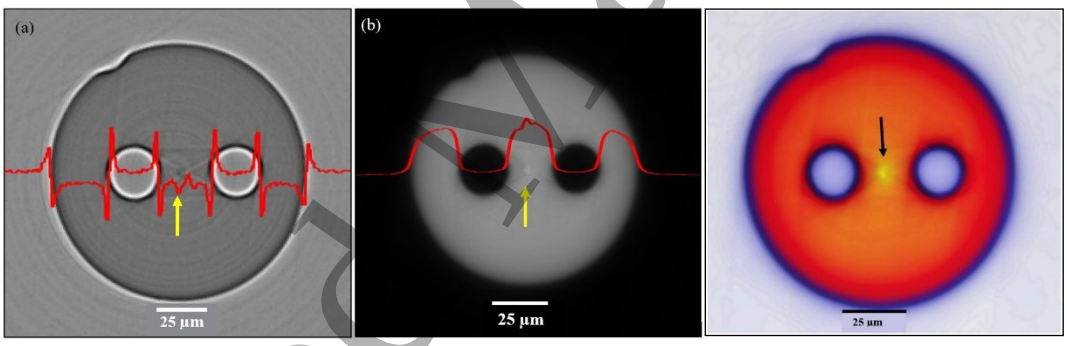

Figure 3. Slice of FBP reconstruction (a) without phase retrieval, (b) with phase retrieval and (c) phase retrieval and a colored label. The red line shows the intensity gray level profile and the arrows indicate the core.

An important step before making the image segmentation was to test the different image filters to get the best border definition without loss of the real information. For this work, the best results were found using non-local means filter implemented by Avizo

software. In figure 4 one can compare the fiber slices images without (fig. 4a) and with (fig. 4b) application of the non-local means image filter. The result is a "denoised" image with well-defined borders.

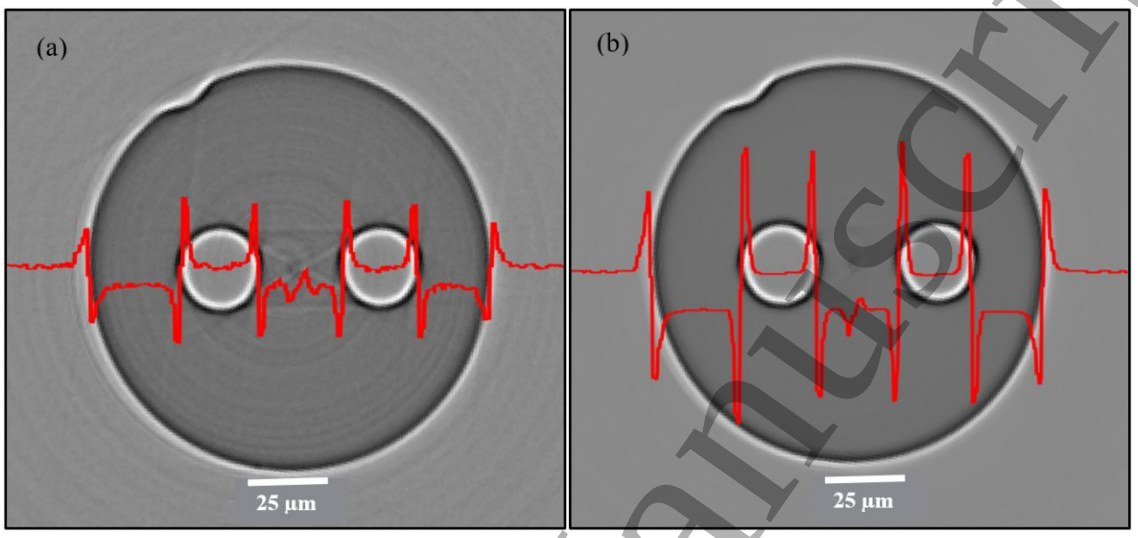

Figure 4. Single slice of the fiber (a) without image filter and (b) with image non-local means filter. The red line indicates the intensity gray level profile.

Image segmentation was applied to separate and to measure the fiber matrix and the hollow volumes individually. Measurements related to the size of the fiber and the holes were carried out in the first analysis. The segmentation provided the separation of the whole fiber into three objects labeled as the fiber matrix, the hole 1 and the hole 2. Figure 5a shows the fiber matrix external surface and Figure 5b shows an image containing the three regions: the translucent fiber matrix and the hollow volumes.

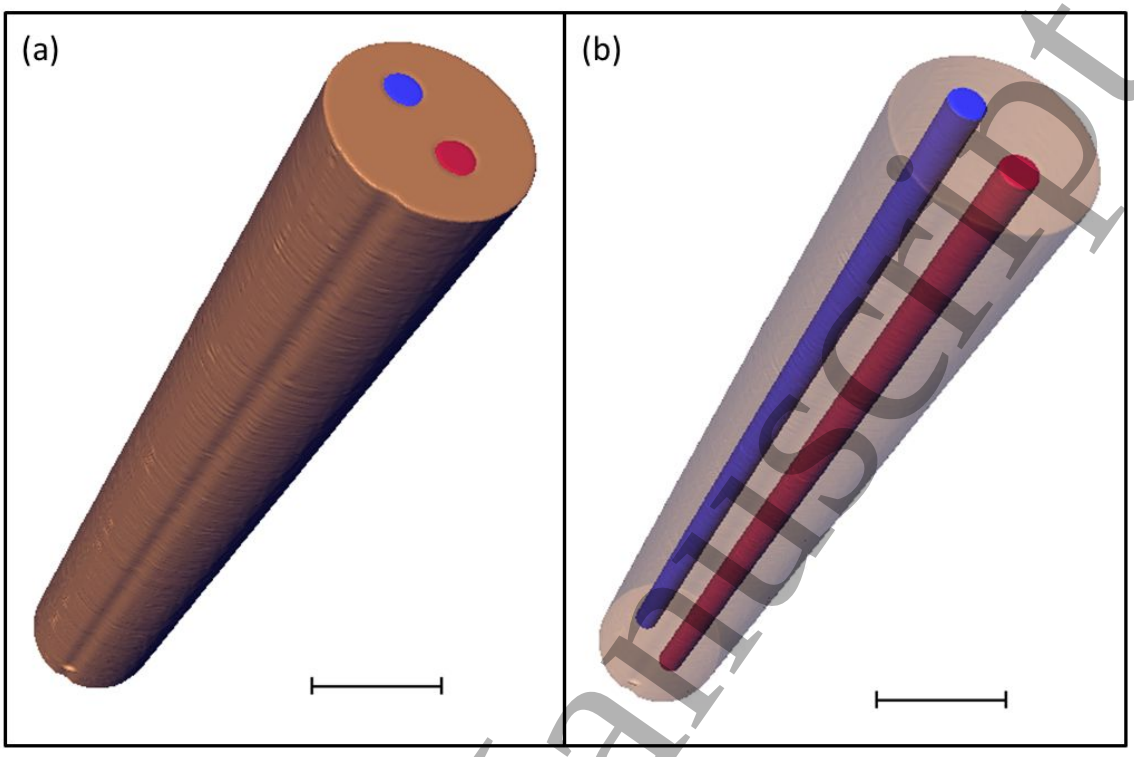

Figure 5. Views of (a) fiber matrix external surface and (b) translucent fiber matrix, hole 1 (red) and hole 2 (blue). Scale bar: 100 μm.

The Avizo *Label Analysis* module allows the computation of a set of measurements for each object and when meaningful, for each slice. The information obtained on the fiber geometry was the Feret's diameter (FD), equivalent diameter and eccentricity of each object. The equivalent diameter is a parameter calculated from the surface area treated as an ellipse with semi-major axis (a) semi-minor axis (b) and correspondent b/a ratios. FD is a measurement used to obtain maximum and minimum values of the diameter for each direction. Using a step-size of one degree, 180 values of diameters were obtained [33].

The largest FD for the fiber matrix is 129.29 µm and the smallest is 125.46 µm. The global average for the fiber matrix is 128 µm with a SD of 1 µm, resulting in a CV of 0.46 %. Hole 1 is the smallest of the two holes with the average of its equivalent diameter calculated by the area surface equals to 23.88 µm, SD of 0.06 µm and CV of 0.25%, while the average value of the b/a ratio and the SD of the ratio are 0.971 and 0.007, respectively. FD ranges from 22.96 µm to 25.51 µm. Figure 6 shows graphically the results of the equivalent diameter and the b/a ratio per slice of the hole 1.

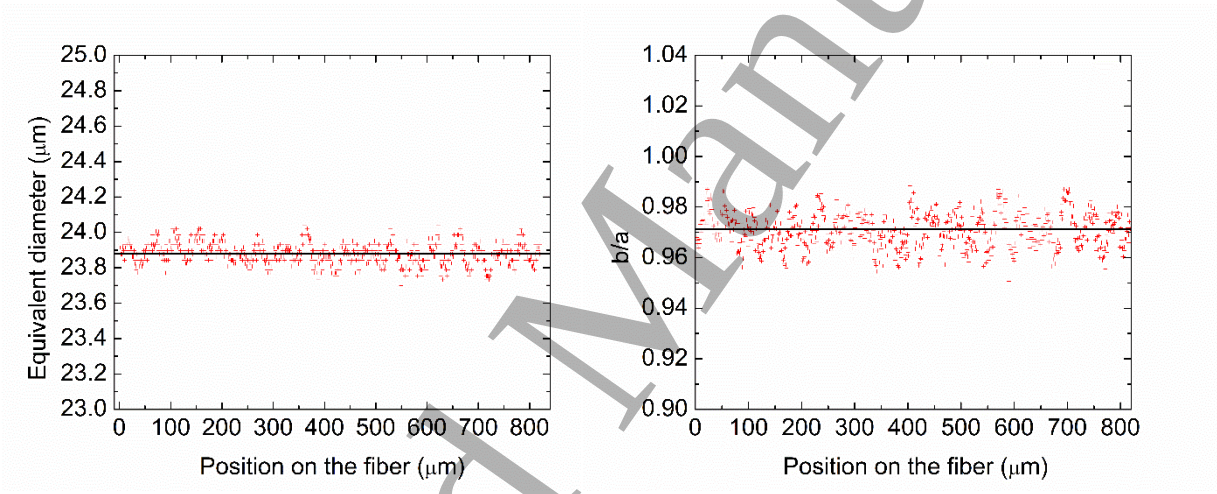

Figure 6. Equivalent diameter (left) and b/a ratio (right) for hole 1 along the length of the fiber. Black line crossing each graphic represents the average value.

The largest Feret's diameter for hole 2 is 27.50 µm and the smallest is 23.77 µm. Hole 2 has an equivalent diameter of 24.88 µm with SD of 0.09 µm, resulting in a CV of 0.36%. The value of the b/a ratio and the respective SD are 0.957 and 0.012. Figure 7 presents the distribution of the equivalent diameter and the b/a ratio for hole 2.

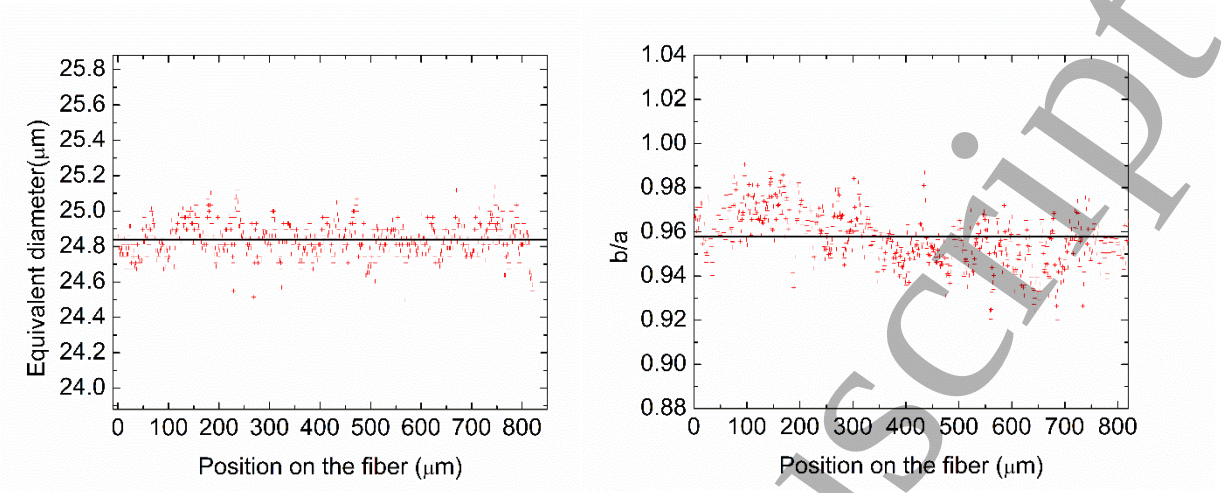

Figure 7. Equivalent diameter (left) and b/a ratio (right) for hole 2 along height of the fiber. Black line crossing each graphic represents the average value.

A critical geometric parameter is the distance between the borders of the holes and the center of the fiber since it influences the time for the creation of the second-order nonlinearity. To determine the distance from the border of the hole to the center of the fiber, we subtracted the coordinates of the borders (closest fiber matrix centroid) from the fiber centroid position for each slice. Figure 8 shows the distribution of the distance from the border of the holes to the center of the fiber. The average distance from hole 1 to the center of fiber is 16.44 μm with SD of 0.10 μm and CV of 0.6%. The border of hole 1 to the center of the fiber distances range from 16.19 μm to 16.67 μm with an amplitude of 0.48 μm, i.e., less than a pixel size. The average distance from hole 2 to the fiber center is 9.29 μm with SD of 0.26 μm and CV of 2.8% indicating less uniformity for this distance when compared with hole 1, ranging from 8.32 μm to 9.79 μm, resulting in amplitude variation of 1.47 μm.

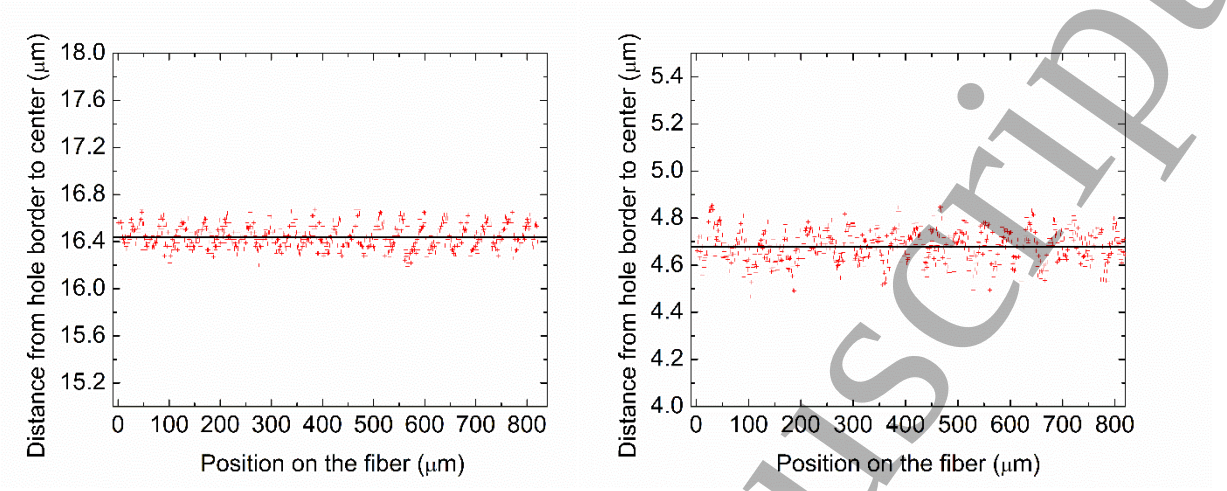

Figure 8. Distribution of the distance from hole 1 (left) and hole 2 (right) borders to the center of the fiber. Black lines are the average values.

The periodic sawtooth-like profile observed in figure 8 is a direct effect of the segmentation process. The segmentation process uses the threshold gradient between the object to be segmented and the other parts. The software selects, based on the gradient image, where the border is located. In our case, after approximately 50 slices, the software corrects the border to half pixel-down. The profile is evident just because the fiber has a very regular structure with well-defined borders.

3.3. COMSOL Simulation

The TDSP was chosen to perform the simulation due to the low concentration of Na^+, Li^+ and H^+ in the fiber matrix (approximately 1 ppm). In the thermal poling process, the ions will move along the fiber matrix due to the diffusion caused by the high

temperature (265 °C). As the movement of the ions is, in principle, aleatory, the ions are drifted by an external electric field generated from the application of high voltage (~5 kV) in the fiber electrodes. COMSOL Multiphysics solve all problems using the finite elements method. Thus, to achieve accurate results, a dense mesh needs to be established over the whole cross-section of the fiber. The model will solve the equation (1) for each subdivision of the geometry and then sum all to give the results that are shown in Figure 1.

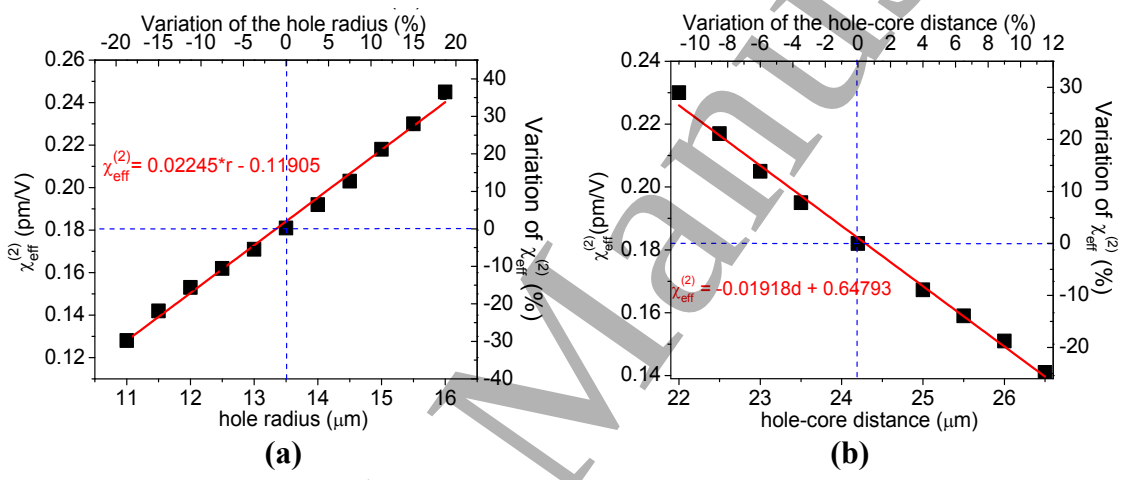

Figure 9: (a) Dependence of $\chi^{(2)}_{eff}$ on the variation of the radius of the holes when the center-to-center (holes to core of the fiber) distances are fixed at 24.2μm and 29.2 μm, respectively. **(b)** Dependence of $\chi^{(2)}_{eff}$ on the variation of the distance from hole 1 surface to the core fiber. The black dots represent the maximum $\chi^{(2)}_{eff}$ simulated, the red line represents the linear fitting of the simulated data. In both graphs, the blue dashed lines show the original values of F051007-1C fiber.

Analyzing figure 9a one can note that the value of $\chi^{(2)}_{eff}$ varies approximately 0.023 pm/V per μm, which means dependence of 12.3% per μm. Analyzing figure 9b and taking into account that in the original position the value of $\chi^{(2)}_{eff}$ = 0.18 pm/V [6], the variation of $\chi^{(2)}_{eff}$ due the fluctuations of the distance between the hole's surfaces to the core of the

fiber is estimated to be (0.02 pm/V)/μm, which means a variation of approximately 10.5% per μm. This critical dependence shows the importance of have all sizes, shapes, and distances among the microstructures uniform.

4. Discussion

By using the three-dimensional analysis provided by SR micro-CT technique one can achieve much more representative results despite the slightly poorer resolution, since many more slices can be quantified for each sample. Bidimensional SEM images were obtained from eight serial sections of a 3 cm length sample. After SEM analysis, another sample of the same fiber with length of 0.820 mm was randomly selected for micro-CT scanning. Through the 3D volume of the sample imaged, 1000 cross-sectional images (virtual slices) were analyzed. The results obtained to the fiber F051007-1C showed that the distance of the hole to the core of this fiber varies with a SD equal to 0.6% and the radii of the holes have a variation equal to 0.3%, both below the limit imposed by the pixel size (1 pixel = 0.82 μm). Now, with the statistics of the measured values, it is possible to estimate the fluctuation of the value of V_π (and, consequently, the fluctuation of the obtained nonlinear susceptibility $\chi^{(2)}_{eff}$) of the poled components. In the case of the fiber used in this work, due to the linear dependence of V_π and $\chi^{(2)}_{eff}$, the fluctuation of the value of V_π is ± 1.71%. Knowing how much the value of V_π fluctuates, give us not only the perspective to improve the poling process but also to improve the geometry and the fabrication process of the microstructures of the specialty optical fiber. It also makes it possible to estimate the degree of repeatability that a commercial product could withhold.

It should be stressed that the 3D imaging technique is not capable of providing alone the information needed to estimate the reproducibility of the second-order nonlinearity induced in poled fibers. A sequence of image processing techniques was also required for

data analysis and retrieval of information. We showed that phase-contrast followed by phase retrieval allowed for the precise location of the core of the fiber and the borders of the holes. Likewise, the denoising of the images lead to accurate segmentation and thus accurate quantification. Finally, the possibility of quantification of the different diameters throughout the fiber length in slices with thicknesses smaller than 1 μm allowed evaluating the effect of the geometrical features of the microstructures present in the specialty fibers. All these contribute to evaluating the variability of performance of poled fibers due to the geometric variation, impacting on the performance parameter Vπ. A comparison of the diameters measured by the conventional SEM and our micro-CT are statistically compatible and validate the latter technique.

5. Conclusion

As an alternative to conventional characterization methods of the specialty fiber optics, in this work we proposed the use of X-ray phase-contrast synchrotron micro-CT to perform a 3D high-resolution qualitative assessment of the fiber microstructure. This results in detailed knowledge about its important morphometric parameters, in a non-destructive fashion. The three-dimensional analysis is one of the main advantages of this work when compared with the most common techniques such as scanning electron microscopy and visible light microscopy.

This technique showed the possibility to unveil microstructural changes induced by the manufacture of the fibers, which can lead to significant alteration in its performance in electrooptical applications. The distance from the core of the fibers to the borders of the holes could be precisely measured, as well as the diameters of the fiber and its holes. In addition, it was also possible to establish the variation of the above-mentioned measurements throughout the fiber, with a virtual slicing down to 820 nanometers with subsequent quantification of the parameters. In the particular case of the fiber F051007-1C, the 3D analysis of the microstructures of the fiber showed that the fluctuation of the value of V_π is ± 1.71%. The fact that the fluctuation of the value of V_π can be measured from a single dataset acquisition represents a great advantage of micro-CT technique when it is compared e.g. with SEM technique. To obtain the same statistical result, it would need at least 1000 images of the cross-section of the optical fiber taken in different points making the process expensivier and time consuming.

Our results helps estimating the behavior of the nonlinear susceptibility $\chi^{(2)}_{eff}$ of the fiber in a precise and fast manner. This information can help the manufacturer improve the quality of the fibers and establish quality control. Although the cost of the use of synchrotron sources is still high when compared with other techniques, new generations of desktop (nano)micro-CT are already available, providing very reliable results in a considerably lower cost.

Acknowledgments

The authors thank to IMX team from LNLS for the support during the project measurements and CNPEN for financial support. They also thank the support from the Conselho Nacional de Desenvolvimento Científico e Tecnológico-CNPq, H2020 ITN FINESSE (722509), K. A. Wallenberg Foundation (2016.0104) and the Swedish Research Council (2015.04346). This study was financed in part by the Coordenação de Aperfeiçoamento de Pessoal de Nível Superior - Brasil (CAPES) - Finance Code 001 and Fundação de Amparo à Pesquisa do Estado do Rio de Janeiro (FAPERJ).

References

[1] A. R. Camara, J. M. B. Pereira, O. Tarasenko, W. Margulis, I. C. S. Carvalho, Optical creation and erasure of the linear electrooptical effect in silica fiber**,** Opt. Express 23 (2015) 18060-18069. https://doi.org/10.1364/OE.23.018060.

[2] De Lucia, F., & Anthony Sazio, P. J. (2019). Optimized optical fiber poling configurations. Optical Materials: X, 100016. doi:10.1016/j.omx.2019.100016

[3] Mizunami, T., Sasaki, R., & Kimura, T. (2016). Effect of fiber stretch on quasi-phase-matching for second-harmonic generation in thermally poled twin-hole silica-glass fiber. *Thin Solid Films*, 47–51, 614. doi:10.1016/j.tsf.2016.04.022

[4] Chung, D. D. L., & Xi, X. (2020). Electric poling of carbon fiber with and without nickel coating. *Carbon*, 25-35, 162. doi:10.1016/j.carbon.2020.02.019

[5] M. Malmström, O. Tarasenko, W. Margulis, Pulse selection at 1 MHz with electrooptic fiber switch, Opt. Express 20 (2012) 9465-9470. https://doi.org/10.1364/OE.20.009465.

[6] A. Michie, I. Bassett, J. Haywood, Electric field and voltage sensing using thermally poled silica fibre with a simple low coherence interferometer, Meas. Sci. Technol. 17 (2006) 1229–1233. https://doi.org/10.1088/0957-0233/17/5/S47.

[7] O. Tarasenko, W. Margulis, Electro-optical fiber modulation in a Sagnac interferometer, Opt. Lett. 32 (2007) 1356-1358. https://doi.org/10.1364/OL.32.001356.

[8] W. Margulis, O. Tarasenko, N. Myrén, Who needs a cathode? Creating a second-order nonlinearity by charging glass fiber with two anodes, Opt. Express 17 (2009) 15534-15540. https://doi.org/10.1364/OE.17.015534.

[9] Zhang, Y., Sun, Y., Cai, L., Gao, Y., & Cai, Y. (2020). Optical fiber sensors for measurement of heavy metal ion concentration: A review. Measurement, 107742. doi:10.1016/j.measurement.2020.107742

[10] Zhang, J., Liu, J., Huang, H., Hu, B., Zhang, Y., Zhang, C., & Ma, S. (2020). Preparation and property study on high 248 nm light transmittance optical fiber coating. Optical Fiber Technology, 57, 102151. doi:10.1016/j.yofte.2020.102151

[11] Villarraga-Gómez, H., Lee, C., & Smith, S. T. Dimensional metrology with X-ray CT: A comparison with CMM measurements on internal features and compliant structures. Precision Engineering, 51, 291–307, 2018. https://doi.org/10.1016/j.precisioneng.2017.08.021

[12] Brunke, O., Santillan, J., & Suppes, A. (2010). Precise 3D dimensional metrology using high-resolution x-ray computed tomography (μCT). Developments in X-Ray Tomography VII. doi:10.1117/12.861354.

[13] Kourra, N., Warnett, J. M., Attridge, A., Dahnel, A., Ascroft, H., Barnes, S., & Williams, M. A. (2016). A metrological inspection method using micro-CT for the analysis of drilled holes in CFRP and titanium stacks. The International Journal of Advanced Manufacturing Technology, 88(5-8), 1417–1427. doi:10.1007/s00170-016-8691-4

[14] A. E. Scott, M. Mavrogordato, P. Wright, I. Sinclair, S. M. Spearing. In situ fibre fracture measurement in carbon–epoxy laminates using high resolution computed tomography, Compos. Sci. Technol., 71(12) (2011)1471-1477. https://doi.org/10.1016/j.compscitech.2011.06.004

[15] Villarraga-Gómez, H., Herazo, E. L., & Smith, S. T. (2019). Progression of X-ray computed tomography from medical imaging to current status in dimensional metrology. Precision Engineering, 60, 544-569, 2019. doi:10.1016/j.precisioneng.2019.06.007

[16] Kruth, J. P., Bartscher, M., Carmignato, S., Schmitt, R., De Chiffre, L., & Weckenmann, A. (2011). Computed tomography for dimensional metrology. CIRP Annals, 60(2), 821–842. doi:10.1016/j.cirp.2011.05.006

[17] S. R. Sandoghchi, G. T. Jasion, N. V. Wheeler, S. Jain, Z. Lian, J. P. Wooler, R. P. Boardman, N. Baddela, Y. Chen, J. Hayes, E. Numkam Fokoua, T. Bradley, D. R. Gray, S. M. Mousavi, M. Petrovich, F. Poletti, D. J. Richardson, X-ray tomography for structural analysis of microstructured and multimaterial optical fibers and preforms. Optics Express, 22(21) (2014) 26181-26192. https://doi.org/10.1364/OE.22.026181

[18] L. K. Batte, R. W. Sullivan, V. Ranatunga, K. Brown, Impact response in polymer composites from embedded optical fibers, Journal of Composite Materials 52(25) (2018) 3415-3427. https://doi.org/10.1177/0021998318763274

[19] Brunke, O., Brockdorf, K., Drews, S., Müller, B., Donath, T., Herzen, J., & Beckmann, F. (2008). Comparison between x-ray tube-based and synchrotron radiation-based μCT. Developments in X-Ray Tomography VI. doi:10.1117/12.794789

[20] Wirjadi, O., Godehardt, M., Schladitz, K., Wagner, B., Rack, A., Gurka, M., … Noll, A. (2014). *Characterization of multilayer structures in fiber reinforced polymer employing synchrotron and laboratory X-ray CT. International Journal of Materials Research, 105(7), 645–654.* doi:10.3139/146.111082

[21] Kastner, J., Harrer, B., Requena, G., & Brunke, O. (2010). A comparative study of high resolution cone beam X-ray tomography and synchrotron tomography applied to Fe- and Al-alloys. NDT & E International, 43(7), 599–605. doi:10.1016/j.ndteint.2010.06.004

[22] P. Cloetens, W. Ludwig, J. Baruchel, D. van Dyck, J. van Landuyt, J. P. Guigay and M. Schlenker, Holotomography: quantitative phase tomography with micrometer resolution using hard synchrotron radiation x rays, Appl. Phys. Lett. 75 (1999) 2912-2924. https://doi.org/10.1063/1.125225.

[23] A. Camara, O. Tarasenko, W. Margulis, Study of thermally poled fibers with a two-dimensional model, *Opt. Express* 22 (2014) 17700-17715. https://doi.org/10.1364/OE.22.017700.

[24] F. De Lucia, R. Bannerman, N. Englebert, M. M. A. N. Velazquez, F. Leo, J. Gates, S. P. Gorza, J. Sahu, P. J. A. Sazio, Single is better than double: theoretical and experimental comparison between two thermal poling configurations of optical fibers, Opt. Express 27(20) (2019) 27761-27776. https://doi.org/10.1364/OE.27.027761.

[25] L. Huang, H. An, J. G. Hayashi, G. Ren, A. Stefani, S. Fleming, Thermal poling of multi-wire array optical fiber, Opt. Express 26(2) (2018) 674-679. https://doi.org/10.1364/OE.26.000674.

[26] S. Wang, Z. Chen, N. Chen, W. Xu, Q. Hao, S. Liu, Thermal poling of new double-hole optical fibers, Appl. Sci., 9(11) (2019) 2176. https://doi.org/10.3390/app9112176.

[27] M. Kampschulte, A. C. Langheinirch, J. Sender, H. D. Litzlbauer, U. Althöhn, J. D. Schwab, E. Alejandre-Lafont, G. Martels, G. A. Krombach. Nano-Computed Tomography: Technique and Applications. Rofo, 188(2) (2016)146-54.

[28] G. J Q. Vasconcelos; E. X. Miqueles; G. S. R. Costa. Responsive alignment for X-ray tomography beamlines. Journal of Synchrotron Radiation, 25(6) (2018) 1-6. https://doi.org/10.1107/S1600577518012201.

[29] D. Paganin, S. C. Mayo, T. E. Gureyev, P. R. Wilkins, S. W. Wilkins, Simultaneous phase and amplitude extraction from a single defocused image of a homogeneous object, Journal of Microscopy. 206 (2002) 33–40. https://doi.org/10.1046/j.1365-2818.2002.01010.x.

[30] E. X. Miqueles, E. S. Helou. Fast Backprojection Operator for Synchrotron Tomographic Data. In: Russo G., Capasso V., Nicosia G., Romano V. (eds) Progress in Industrial Mathematics at ECMI 2014. ECMI 2014. Mathematics in Industry, Springer, 22(2014) 243-252. https://doi.org/10.1007/978-3-319-23413-7_32.

[31] E. X. Miqueles, E. S. Helou, A. R. de Pierro, Generalized backprojection operator: fast calculation. J. Phys.: Conf. Ser. 490 (2014) 012148. https://doi.org/10.1088/1742-6596/490/1/012148.

[32] L. Vincent and P. Soille, "Watersheds in digital spaces: an efficient algorithm based on immersion simulations," in *IEEE Transactions on Pattern Analysis and Machine Intelligence*, vol. 13, no. 6, pp. 583-598, June 1991, doi: 10.1109/34.87344.

[33] W. H. Walton, Feret's Statistical Diameter as a Measure of Particle Size, Nature 162 (1948) 329–330. https://doi.org/10.1038/162329b0.
